CHEMISTRY OF MATERIALS
Cite This: Chem. Mater. 2018, 30, 4508−4514
Article
pubs.acs.org/cm

$Mn_2(Fe_{0.8}Mo_{0.2})MoO_6$: A Double Perovskite with Multiple Transition Metal Sublattice Magnetic Effects

Man-Rong Li,*[,†,‡] Peter W. Stephens,[§] Mark Croft,[∥] Zheng Deng,[⊥] Wenmin Li,[⊥] Changqing Jin,[⊥] Maria Retuerto,[†] Jason P. Hodges,[#] Corey E. Frank,[†] MeiXia Wu,[‡] David Walker,[¶] and Martha Greenblatt*[,†]

[†]Department of Chemistry and Chemical Biology, Rutgers, The State University of New Jersey, 610 Taylor Road, Piscataway, New Jersey 08854, United States

[‡]MOE Key Laboratory of Bioinorganic and Synthetic Chemistry, School of Chemistry, Sun Yat-Sen University, Guangzhou 510275, China

[§]Department of Physics & Astronomy, State University of New York, Stony Brook, New York 11794, United States

[∥]Department of Physics & Astronomy, Rutgers, The State University of New Jersey, 136 Frelinghuysen Road, Piscataway, New Jersey 08854, United States

[⊥]Beijing National Laboratory for Condensed Matter Physics Institute of Physics, Chinese Academy of Sciences, Beijing 100090, China

[#]Spallation Neutron Source, Oak Ridge National Laboratory, Oak Ridge, Tennessee 37831, United States

[¶]Lamont Doherty Earth Observatory, Columbia University, 61 Route 9W, P.O. Box 1000, Palisades, New York 10964, United States

Supporting Information

ABSTRACT: Transition-metal-only perovskite oxides can introduce additional magnetic functionality with robust magnetoelectric properties but are rare. In this work we prepared a new transition-metal-only perovskite $Mn_2(Fe_{0.8}Mo_{0.2})MoO_6$ at high pressure and temperature. Uniquely, $Mn_2(Fe_{0.8}Mo_{0.2})MoO_6$ was discovered as a line phase upon composition modulation that was motivated from the above-room-temperature multiferroic Mn_2FeMoO_6 corundum phase. It exhibits ferrimagnetic Fe−Mo sublattice (T_C = 194 K) and Mn sublattice antiferromagnetic (T_m ∼ 45 K) transitions. Below T_m the two sublattice orderings are coupled and give rise to canted components in both. A first-order field-induced transition is also observed below 45 K. $Mn_2(Fe_{0.8}Mo_{0.2})MoO_6$ is a Mott variable range hopping semiconductor. These findings for the first time show that either an exotic perovskite or a corundum phase can be achieved by composition modulation besides the pressure effect.

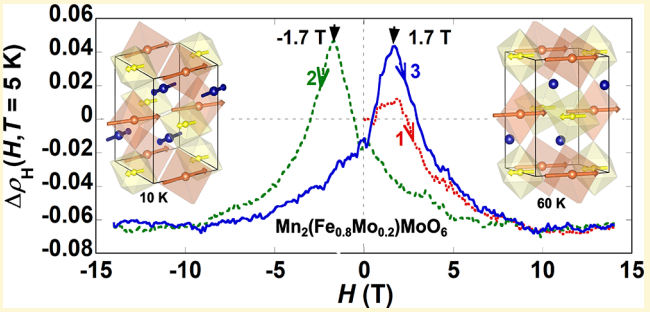

1. INTRODUCTION

Exotic perovskite oxides with transition-metal ions at both A- and B-sites are expected to introduce additional magnetic functionality with possible robust magneto-electric properties.[1−10] The A-site ordered $AA'_3B_4O_{12}$ quadruple perovskites usually have transition-metal ions in 3/4 of the A-sites (A′) as in $LaCu_3Fe_4O_{12}$ and $CaCu_3Fe_2Re_2O_{12}$, which show above-room-temperature reversible metal−insulator transition and spin-polarized half-metallic state, respectively.[3,4] Although $A_2BB'O_6$-type double perovskites Mn_2BSbO_6 (B = Cr, Fe) possess Mn^{2+} (high-spin d^5) at the A-sites, they are less promising (antiferromagnetic (AFM) order ∼ 55 K) compared with the above-mentioned quadruple perovskites,[11,12] likely due to the nonmagnetic B′-site Sb^{5+}. Thus, the design and synthesis of transition-metal-only perovskites with enhanced magnetic interactions are desirable. To the best of our knowledge, so far only six transition-metal-only perovskite oxides have been prepared, including $MnVO_3$, $ACu_3V_4O_{12}$ (A = Mn, Cu), ζ-Mn_2O_3, and Mn_2BReO_6 (B = Mn, Fe). Metallic $MnVO_3$ is the only ABO_3 simple perovskite.[1] Quadruple perovskites $ACu_3V_4O_{12}$ (A = Mn, Cu) demonstrate interesting cationic rattling of the 12-coordinated Mn^{2+} and Cu^{2+} at the A-sites.[13,14] The ζ-Mn_2O_3 in a distorted quadruple perovskite structure $(Mn^{2+}(Mn^{3+})_3(Mn^{3.25+})_4O_{12})$ is a semiconductor with direct narrow bandgap and switchable *p*−*n* electrical conduction.[5,6] Mn_2FeReO_6[7,8] and Mn_2MnReO_6[9,10] are the only two $A_2BB'O_6$ double perovskites: Mn_2FeReO_6 is a ferrimagnetic (FiM) half-metal (Curie temperature T_C ∼ 520 K) that shows giant

Received: January 18, 2018
Revised: June 1, 2018
Published: June 1, 2018

DOI: 10.1021/acs.chemmater.8b00250
Chem. Mater. 2018, 30, 4508−4514

positive magnetoresistance of 220% at 5 K and 8 T,[7,8] while Mn_2MnReO_6 is a one-dimensional variable-range hopping semiconductor with AFM transition at ~ 110 K.[9,10]

In this work, we prepared a new transition-metal-only double perovskite $Mn_2Fe_{0.8}Mo_{1.2}O_6$ (MFMO) under high pressure via the B-site composition modulation motivated by the recent synthesis at high pressure (8 GPa) of Mn_2FeMoO_6 and the findings of exotic properties of this new phase.[15,16]

2. EXPERIMENTAL DETAILS

Synthesis. Polycrystalline $Mn_2Fe_{0.8}Mo_{1.2}O_6$ was prepared from a stoichiometric mixture of MnO (99.99%, Alfa Aesar), Fe (99.998%, Alfa Aesar), Fe_2O_3 (99.998%, Alfa Aesar), and MoO_3 (99.8%, Alfa Aesar) at 1623 K for 1 h under 8 GPa in a Walker-type Multi Anvil Press and then quenched to room temperature by turning off the voltage supply to the resistance furnace as reported in our previous work.[7,10,16−22] The pressure is maintained during the temperature quenching and then decompressed slowly in 8−12 h.

Powder X-ray and Neutron Diffraction. Room-temperature powder X-ray diffraction (PXD) data were collected on a Bruker D8 Advance Diffractometer (Cu K_α, λ = 1.5418 Å) with a SOL-X solid state detector. Room-temperature synchrotron powder X-ray diffraction (SPXD) data were recorded on beamline X-16C (λ = 0.70019 Å) at the Brookhaven National Synchrotron Light Source (NSLS) in the U.S. Powder neutron diffraction (PND) data were collected on an about 500 mg polycrystalline sample at 10, 60, and 300 K on the POWGEN instrument at the Spallation Neutron Source at Oak Ridge National Laboratory (U.S.). The magnetic structure symmetry analysis was performed with ISODISTORT software.[23] The EXPGUI interface of the GSAS program[24] was used for Rietveld refinement[25] of the atomic and magnetic spin structures. Representations of the crystal and spin structures were made with VESTA-3.[26]

X-ray Absorption Near-Edge Spectroscopy. Mn− and Fe−K X-ray absorption near-edge spectroscopy (XANES) data were collected in both the transmission and fluorescence mode with simultaneous standards. The Mo XANES was collected in fluorescence mode in a He-atmosphere-chamber with standards run in temporal proximity. All of the spectra were fit to linear pre- and postedge backgrounds and normalized to the unity absorption step across the edge.[7,27−33] All of the XANES was performed on beamline X-19A at the Brookhaven NSLS with a Si-111 double-crystal monochromator.

Magnetism and Magnetotransport. Magnetization measurements were carried out with a Quantum Design superconducting quantum interference device (SQUID) magnetometer. The magnetic susceptibility (χ) was measured in zero field cooled (ZFC) and field cooled (FC) conditions under 0.1, 1, and 5 T applied magnetic field (H) for temperatures ranging from 5 to 400 K. Isothermal magnetization curves were obtained at 5, 10, 100, 170, 200, 220, 300, and 400 K under an applied magnetic field varying from −5 to 5 T. The magnetotransport properties were measured on a pellet sample with the standard four-probe technique in a physical property measurement system (PPMS) from Quantum Design at 0 and 7 T, respectively. The magnetic-field-dependent conductivity variation was measured between −14 and 14 T at 5 K.

3. RESULTS AND DISCUSSION

3.1. Line Phase and Crystal Structure. The Ni_3TeO_6-type multiferroic Mn_2FeMoO_6 is a highly spin-polarized above-room-temperature FiM (T_C ~ 340 K) semiconductor; it shows an unexpected low-temperature (150−300 °C) cationic rearrangement at ambient pressure, accompanied by a Ni_3TeO_6-to-ordered-ilmenite structural transition and dramatic physical property changes.[15,16] These findings inspired further composition modulations in Mn_2FeMoO_6 for optimal physical properties as in Sr_2FeMoO_6 and $Sr_2Fe_{1+x}Mo_{1-x}O_6$.[32,34] However, attempts to prepare $Mn_2Fe_{1+x}Mo_{1-x}O_6$ ($-0.3 \le x \le 0.33$) solid solutions up to 8 GPa and 1623 K were unsuccessful. PXD data show that only a double perovskite-related line phase MFMO can be achieved at $x = -0.2$ besides the Ni_3TeO_6-type Mn_2FeMoO_6 ($x = 0$) (Figure S1 in Supporting Information (SI)). Detailed analysis of the SPXD and PND data of MFMO collected at 300 K indicates a distorted monoclinic $P2_1/n$ phase (a = 5.222(1) Å, b = 5.382(1) Å, c = 7.605(1) Å, β = 90.04(1)°, V = 213.72(1) Å^3), which yielded a good fit (R_p/R_{wp} = 6.81/3.19%) in a combined SPXD and PND refinement with the structural model of Mn_2MReO_6 (M = Mn, Fe)[7−10] and Mn_2MSbO_6 (M = Sc, Fe, Cr) perovskites[11,12,35] as shown in Figures 1A and S2. The final

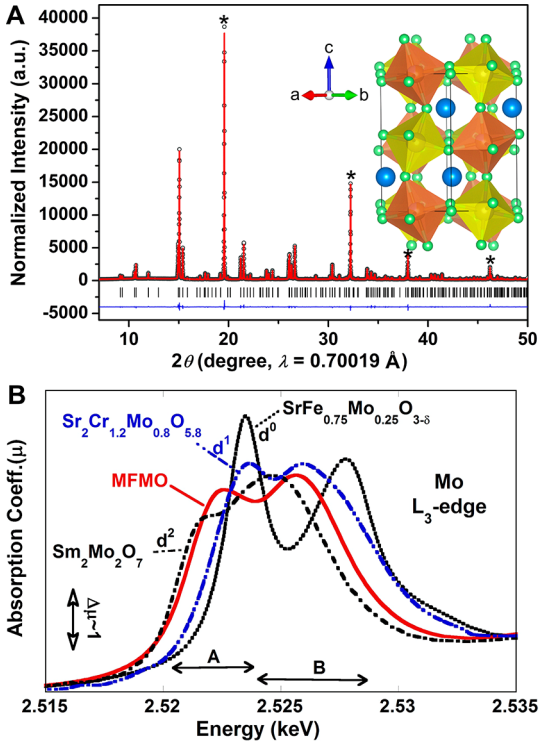

Figure 1. (A) SPXD plots of MFMO from combined refinements in monoclinic $P2_1/n$ structure at room temperature. The asterisks (*) denote the peaks of diamond internal standard. The inset presents the crystal structure of MFMO showing rock-salt ordering of $(Fe_{0.73(1)}Mo_{0.27(1)})O_6$ and MoO_6 octahedral connections. Mn atoms, blue spheres; O, green spheres; $(Fe_{0.73(1)}Mo_{0.27(1)})O_6$ octahedra, brown; MoO_6 octahedra, yellow. (B) A superimposed comparison of the Mo-L_3 edge of MFMO to those of the d^0/Mo^{6+}-$SrFe_{0.75}Mo_{0.25}O_{3-\delta}$, d^1/Mo^{5+}-$Sr_2Cr_{1.2}Mo_{0.8}O_{5.8}$, and ~ $4d^2$-Mo^{4+}-$Sm_2Mo_2O_7$ standards, indicating $Mo^{4+/5+}$ in MFMO. The double-headed arrows denote the t_{2g}- and e_g-related A and B features respectively based upon the octahedral crystal electric field splitting.

crystallographic data are shown in Table S1. There are no oxygen defects observed during the refinements within the standard uncertainties. The A- and B′- sites are fully occupied by Mn and Mo, respectively, while the B-site is mixed with 73(1)% Fe and 27(1)% Mo, giving the structural formula of $Mn^A{}_2(Fe_{0.73(1)}Mo_{0.27(1)})^BMo^{B'}O_6$, in reasonable agreement with the starting stoichiometry.

The crystal structure of MFMO is presented in the inset of Figure 1A, where Mn is in 8-fold coordination, $(Fe_{0.73(1)}Mo_{0.27(1)})O_6$, and MoO_6 octahedra are in a corner-shared rock-salt arrangement. The average ⟨Mn−O⟩ distance of 2.388 Å is in line with those in isostructural $Mn^{2+}{}_2BB'O_6$ (B = Sc, Cr, Mn, Fe; B′ = Sb, Re) between 2.379 and 2.405 Å, giving

DOI: 10.1021/acs.chemmater.8b00250
Chem. Mater. 2018, 30, 4508−4514

bond valence sums (BVS) of 1.93 as listed in Table S2.[10−12,35] The ⟨($Fe_{0.73(1)}Mo_{0.27(1)}$-O⟩ of 2.021 Å is nearly identical with that of the ⟨Fe−O⟩ in $Mn_2Fe^{3+}Re^{5+}O_6$ (2.022 Å)[7,8] and $Mn_2Fe^{3+}Sb^{5+}O_6$ (2.017 Å),[11] which suggests Fe^{3+}/Mo^{4+} at the Fe/Mo site given their almost identical ionic radius values (0.645 and 0.65 Å for Fe^{3+} and Mo^{4+}, respectively, in octahedral coordination).[36] This gives an average charge of 3.27 at the B-site, comparable with the BVS value of 3.18. Assuming Mn^{2+} at the A-site and ($Fe^{3+}_{0.73(1)}Mo^{4+}_{0.27(1)}$) at the B-site, the B′-site Mo therefore has an average charge of 4.73 (compared to its BVS of 4.58) from a mix of 73% Mo^{5+} and 27% Mo^{4+} according to charge balance. This gives overall 2.0-Mn^{2+}, 0.73-Fe^{3+}, 0.54-Mo^{4+}, and 0.73-Mo^{5+}, namely, $Mn^{2+}_2{}^{A}(Fe^{3+}_{0.73(1)}Mo^{4+}_{0.27(1)})^{B}$-$(Mo^{4+}_{0.27(1)}Mo^{5+}_{0.73(1)})^{B'}O_6$, which has been corroborated by the XANES results shown in Figures 1B and S3−4. The low energy chemical shift and pre-edge features further clearly indicate Mn^{2+} and Fe^{3+} valence states in the Mn− and Fe−K edge XANES in Figures S3 and S4. The Mo−L_3 edge XANES in Figure S5 illustrates both the systematic increase of the A (t_{2g}-related) feature intensity, relative to the B (e_g-related) features, and the increasing chemical shift of the combined A−B feature in the configuration sequence from ∼ $4d^2/Mo^{\sim 4+}$ to $4d^0/Mo^{6+}$. The Mo−L_3 spectra in Figure 1B support the mixed $Mo^{4+/5+}$ valence by both the relative A-feature intensity and A−B feature chemical shift of the MFMO spectrum lying intermediate between those of the ∼d^1/Mo^{5+} ($Sr_2Cr_{1.2}Mo_{0.8}O_{5.8}$) and ∼$4d^2/Mo^{4+}$ ($Sm_2Mo_2O_7$) standard spectra.

3.2. Magnetic Properties at Low Field. Figures 2A and 2B, respectively, present constant field magnetization, $M(T)$, and isothermal magnetization, $M(H)$, measurements on MFMO. For clarity/simplicity the low-field and low-temperature magnetic measurement results will be discussed first to motivate the neutron scattering spin structure measurements. The discussion of the more complex higher-field magnetic behavior will then be returned once the H = 0 spin structure is solidly established.

In Figure 2A, the temperature-dependent ZFC and FC magnetizations of MFMO, for H = 0.1 T, clearly exhibit at least two transitions: an apparently FiM transition at T_C = 194 K and a lower temperature AF-type transition at T_m ∼ 45 ± 3 K. The nonlinear FiM-like $M(H)$ results at T = 100 K and the finite field-induced transition in the $M(H)$ results at T = 5 and 10 K (Figure 2B) support the two-transition-temperature hypothesis. From the above magnetic results the temperatures T = 10 K (below T_m) and T = 60 K ($T_m < T < T_C$) were chosen for H = 0 PND spin structure determination which is discussed in the next section.

3.3. Spin Structures. The magnetic spin structures of MFMO at 10 and 60 K were determined by PND data refinements (Figures 3A, 3B, and S2C, respectively). The

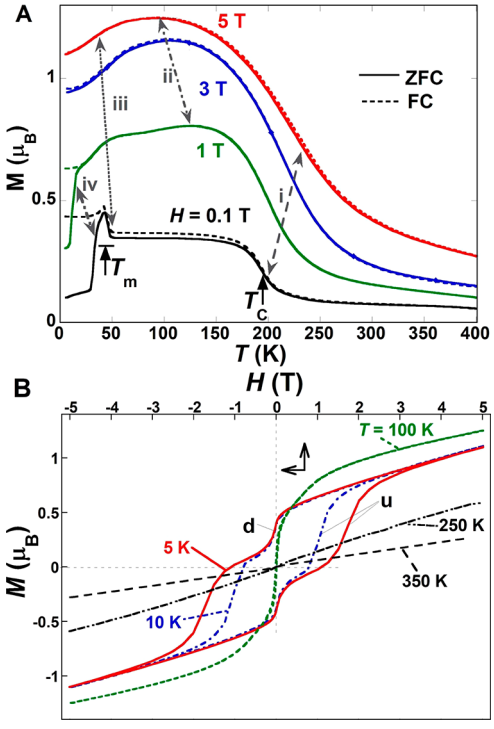

Figure 2. (A) Temperature-dependent magnetization (M) evolution of MFMO between 5 and 400 K at 0.1, 1, and 5 T, respectively, in both ZFC and FC modes. (B) Isothermal $M(H)$ loops of MFMO at 5, 10, 100, 220, and 400 K between 5 and −5 T. Note the hysteretic field-induced transitions upon moving up ("u") and down ("d") in field in the T = 5 and 10 K loops.

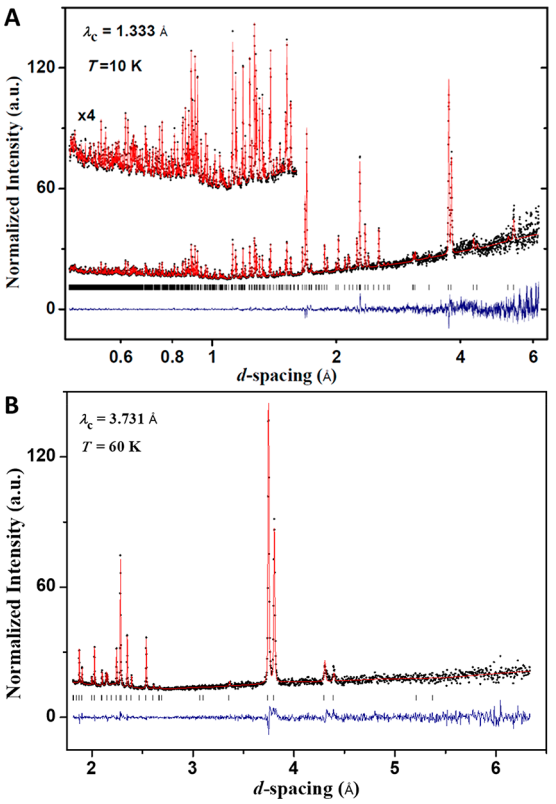

Figure 3. Rietveld refinement plots of the PND data for MFMO of (A) 1.333 Å bank at 10 K and (B) 3.731 Å bank at 60 K. Tick marks show the position of allowed nuclear and magnetic reflections of the perovskite phase.

MFMO magnetic reflections were indexed with the k = (0 0 0) propagation vector and magnetic space group (MSG) $P2_1/n$. Other k = (0 0 0) MSGs $P2_1'/n$, $P2_1'/n'$, and $P2_1/n'$ were discounted as they did not permit all the observed magnetic reflections. The magnetic structures of MFMO at 10 and 60 K are shown in Figure 4. At 60 K antiparallel order of the B and B′ site moments (going forward they will also be referred to as Fe^{3+} and $Mo^{4.7+}$ sites) observed is consistent with spin

DOI: 10.1021/acs.chemmater.8b00250
Chem. Mater. 2018, 30, 4508−4514

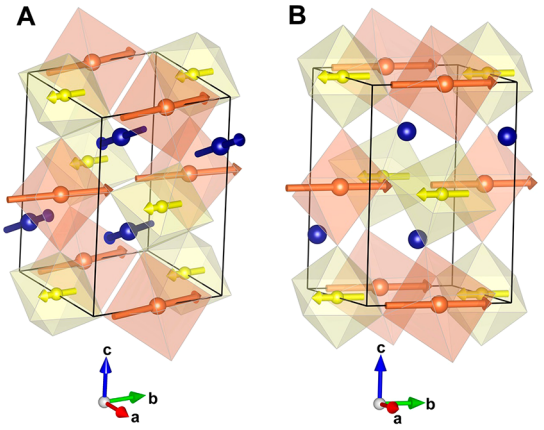

Figure 4. Magnetic structure of MFMO at (A) 10 K and (B) 60 K. Brown = Fe/Mo at B-site, yellow = Mo at B′-site, blue = Mn at A-site.

structures reported for other FiM double perovskites (Figure 4B). The net ferromagnetic component is 1.4 μ_B/f.u. Above T_m ∼ 45 K (the magnetic reorientation transition temperature) the A-site Mn^{2+} spins have not yet ordered as they are partially frustrated by the dominant FiM order of the B/B′ sites.[8] At 10 K the refined spin structure (Figure 4A) has Mn^{2+} moments antiferromagnetically ordered in the m_{xz} plane, and the Fe^{3+} moments (which above T_m were oriented perpendicular along m_y) now exhibit a degree of canting with new alternating $\pm m_x$ component (AFM type, θ_{FeFe} = 20(2)°). Canting of the B/B′ site moments below T_m is also observed for the other closely related Mn^{2+} A-site FiM double perovskites Mn_2FeReO_6 (θ_{FeFe} = 15°) and Mn_2MnReO_6 ($\theta_{BsiteBsite}$ = 15°).[7−10] In our PND refinements, the precise magnitude and direction of canted $Mo^{4.7+}$ moments could not be fully determined at 10 K, and therefore only the m_y ordered spin component was refined. In view of the canting of both the FiM-Fe/Mo and AFM-Mn sublattices in the low-temperature PND-determined phase, this low-field phase will be referred to as the cFiM/AFM in subsequent discussions.

3.4. Magnetic Properties at Finite Field. The neutron diffraction (H = 0) spin structure determinations now provide a sound basis for discussion of the higher-field magnetic results. A tentative $H-T$ magnetic phase diagram is displayed in the SI because it must be regarded only as tentative. Starting from high temperature, the onset of the FiM phase is manifested by the inflection points in the $M(T)$ curves as indicated by the dashed "i" lines in Figure 2A. These i-features are emphasized by the negative peaks in the dM/dT curves in Figure S6A. Here it should be emphasized that model calculations show that the FiM phase onset is a true second-order phase transition only in the H = 0 limit and that the onset is continuous, albeit nonlinear, in the presence of a finite symmetry-breaking magnetic field (see SI for more details).[37,38] The nonlinear S-shaped $M(H)$ loops at T = 100 K (in Figure 2B) and that at T = 170 and 200 K (Figure S6B) are consistent with the FiM transition at T_C.

The spin structure determination below T_m clearly indicated that this transition involved the AFM-type ordering of the Mn sites into a canted-AFM (cAFM) order that is coupled to a reorientation of the Fe−Mo sublattice order into a canted FiM state (cFiM). Moreover, the fact that the Fe-site-canted component has an alternating AFM-like character (see Spin Structures section) further underscores the coupling of the two sublattices.

In dual magnetic site ABO_3 perovskites, magnetic ordering of the B-site at a higher temperature, followed by A-site magnetic ordering at a lower temperature, is not uncommon.[7,8,39−42] Moreover, a complex A/B site magnetic coupling, involving moment competition/frustration/canting, is also a leitmotif in such materials. Understandably, the application of a magnetic field leads to a still more complex interplay of the sites and moment orientations in such multiple-magnetic-sublattice systems. The line "ii" in Figure 2A indicates the local maximum in the $M(T)$ curves at higher magnetic fields. This phenomenon is inferred to reflect the presence of Mn-site AFM correlation coupling to the Fe/Mo site dominated by net magnetization. Indeed, the maximum observed magnetization at H = 5 T occurs near T = 100 K in both the $M(H)$ and $M(T)$ results.

As previously noted, the onset of the coupled cFiM/AFM-type order at T_m is marked by a sharp structure in the H = 0.1 T $M(T)$ curves in Figure 2A. Broader downturn features occur in the magnetization curves for $H \geq 1$ T, at temperatures somewhat less than T_m (see the line "iii" in Figures 2A and S8), and are inferred to indicate the onset of a high-field phase involving cFiM and AFM order and are denoted as HF-cFiM/AFM hereafter (see Figure S8). Field-induced transitions into this HF-cFiM/AFM are discussed below.

For $T < T_m$, the presence of a first-order, field-induced transition from the low-H cFiM/AFM phase into a higher magnetization phase (HF-cFiM/AFM) is emphasized by the 5 and 10 K $M(H)$ loops in Figure 2B and the $M(H)$ curves in Figure S6B. The increasing field metastability limits for the cFiM/AFM to HF-cFiM/AFM transition are identified by "u" in $M(H)$ curves in Figures 2B and S6B. The decreasing field metastability limits for the HF-cFiM/AFM to cFiM/AFM transition are identified by "d" in $M(H)$ curves in Figures 2B and S6B. $M(H)$ and dM/d$H(H)$ curves at 5 K in Figure S7 illustrate the hysteretic field-induced transition around ±1.7 T. It is worth noting that the field-dependent magnetoresistance (Figure 5B) also shows a sharp peak that agrees well with the increasing field cFiM/AFM to HF-cFiM/AFM transition as illustrated in Figure S7. The HF-cFiM/AFM phase extends to the highest field studied at temperatures below ∼30−45 K. The line labeled "iii" in Figure 2B and in the schematic phase diagram in Figure S8 indicates an estimate for the high-temperature border of the HF-cFiM/AFM phase.

Returning to the $M(T)$ curves in Figure 2A the sharp disparities between the FC and ZFC curves, for both the H = 0.1 and 1 T (labeled by "iv" in Figure 2A), should be noted. The temperatures and fields for the step-like changes in these two ZFC $M(T)$ curves, collected by heating from the lowest temperatures after ZFC (i.e., in the cFiM/AFM phase), are included in the phase diagram in Figure S8, and importantly they coincide closely with the magnetic-field-induced metastability limit for the cFiM/AFM to HF-cFiM/AFM transition. This motivates the association of the "iv" features, in the two lowest-field ZFC $M(T)$ curves, with crossing in temperature a metastability limit for the cFiM/AFM to HF-cFiM/AFM transition upon heating.

It should be emphasized that field-induced transition states discussed here will differ depending on the detailed specific crystal-axis orientation of the applied field so that the polycrystalline results in this paper represent an average over such details. Transitions and phase mixtures will also differ for differing crystal axis magnetic field orientations and for differing field/temperature experimental $H-T$ paths. Accordingly, extensive single-crystal studies would be required for a further

DOI: 10.1021/acs.chemmater.8b00250
Chem. Mater. 2018, 30, 4508−4514

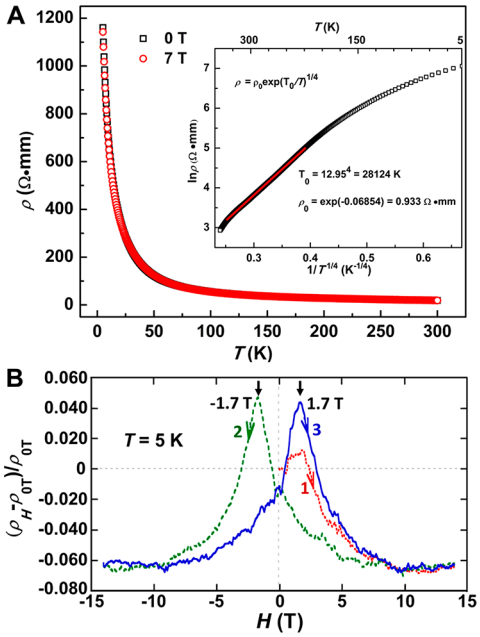

Figure 5. (A) Temperature (T)-dependent resistivity (ρ) plots of MFMO at 0 and 7 T, respectively. Inset shows the linear fit to the plot of ln ρ versus $T^{-1/4}$ above 225 K, indicating Mott's VRH conduction mechanism. (B) Isothermal magnetoresistance at T = 5 K with field paths identified in the sequence: ZFC-prepared, H = 0 to +15 T (path 1, dotted red); +15 to −15 T (path 2, dashed green); and −15 to 15 T (path 3, solid blue). Note that the peaks of the magnetoresistance correspond closely in field to the field-induced transitions in the T = 5 K $M(H)$ and dM/dH results shown in Figure S7.

clarification of the low-temperature H−T phase diagram of this material.

3.5. Magnetotransport and Magnetoresistance. Resistivity (ρ) and magnetoresistance measurements on a polycrystalline MFMO pellet are shown in Figure 5. The resistivity is about 1.15 × 10^3 and 18.9 Ω·mm without applied magnetic field at 5 and 300 K, respectively, which are almost identical with the values measured at 7 T. The overall resistivity shows characteristic semiconducting behavior between 5 and 300 K (Figure 5A). The temperature dependence of ρ was determined by trial fitting the relations $(1/T)^p$, which follows the relation with p = 1/4 between 40 and 260 K and indicates a Mott variable range hopping mechanism $\rho = \rho_0 \exp(T_0/T)^{1/4}$, where T_0 = 281.24 K and ρ_0 = 0.933 Ω·mm.

The magnetic-field-dependent magnetoresistance of MFMO at 5 K gives a peak value of magnetoresistance ratio of ∼ 5% (Figure 5B). Comparing Figure 5B to the dM/dH field-cycling curves in Figure S7 indicates that the sharp peaks in the magnetoresistance, at H = ±1.7 T, occur at the peeks of the dM/dH curves that determine the field-induced transition. Thus, the maximal magnetoresistance in this regime is directly coupled to the maximal phase inhomogeneities that occur at the field-induced cFiM/AFM to HF-cFiM/AFM transition. The reverse HF-cFiM/AFM to cFiM/AFM transition shows up as a much smaller shoulder on the magnetoresistance hysteresis loop. This behavior is similar to what was observed in half-metallic Sr_2FeReO_6 where the peaks in dM/dH and the magnetoresistance occur at the same fields.[43] Sr_2FeReO_6 is however simply a FiM material with no moment on the perovskite A-site.

Insight into the wider temperature range magnetoresistance can be gleaned by calculating the resistivity ratio ρ_0/ρ_H (H = 7 T) using the data in Figure 5A. The results for ρ_0/ρ_H are shown in Figure S9. The utility of resistivity ratio lies in the assumption that the very high-field resistivity (ρ_H) represents a more homogeneous, less resistive state and that the magnetoresistance is dominated by the field suppression of inhomogeneities in the H = 0 resistivity (ρ_0).[44] In Figure S9 the field-induced value of ρ_0/ρ_H first increases with decreasing temperature, reaching a maximum near the FiM T_C. This is presumably due to fluctuation-induced inhomogeneities increasing in magnitude upon approaching the ordering temperature from above. Below T_C, as the magnetic domains grow, ρ_0/ρ_H decreases. In an ∼ 40 K range around T_m the ρ_0/ρ_H becomes less than 1.0 indicating that the magnetic field increases, rather than decreases, inhomogeneities. Finally, at low temperatures ρ_0/ρ_H becomes greater than 1.0 again and is dominated by transiting the field-induced transition and entering the more homogeneous high-field phase. The value of ρ_0/ρ_H from the magnetoresistance curves in Figure 5B, included in Figure S9, supports this analysis. Interpretation of the degree of interdomain/intergrain tunneling versus intergrain affects in the magnetoresistance would be speculative at this stage.

4. CONCLUSIONS

In conclusion, we have prepared the third transition-metal-only double perovskite $Mn_2(Fe_{0.8}Mo_{0.2})MoO_6$ at high pressure via composition modulation. $Mn_2(Fe_{0.8}Mo_{0.2})MoO_6$ is isostructural with Mn_2BReO_6 (B = Mn, Fe). The Fe−Mo sublattice of this compound exhibits a ferrimagnetic transition with T_C = 194 K. The Mn sublattice orders antiferromagnetically at T_m ∼ 45 K. The concomitant canting of the coupled ferrimagnetic (Fe−Mo) and antiferromagnetic (Mn) sublattices is underscored by dubbing T_m as a spin "reorientation" transition. The canted coupling of the two sublattices is still more complex in the presence of magnetic field as emphasized by hysteretic first-order, field-induced phase transition at low temperatures. $Mn_2(Fe_{0.8}Mo_{0.2})MoO_6$ is a Mott variable range hopping semiconductor and exhibits a magnetoresistance coupled to the nonlinear magnetization at low temperature. These transition-metal-rich exotic perovskites can be stabilized at higher pressure over competition with the corundum phases[11,35,45] as observed in the corundum−perovskite transitions in Mn_2BSbO_6 (B = Sc, Fe).[11,35] In contrast, the high-pressure made perovskite phase can also transform into ilmenite structure upon heating at ambient pressure as reported in Mn_2CrSbO_6.[12] So far, only the perovskite phases have been obtained for Mn_2FeReO_6 and Mn_2MnReO_6.[7−10] This finding may be the consequence of the specific spin structures and possible spin−orbit coupling (Re) in Mn_2MnReO_6 and Mn_2FeReO_6 that stabilize a lower-energy perovskite relative to the corundum structure. In the work presented here, the presence of only two line phases, namely, Mn_2FeMoO_6 corundum and $Mn_2(Fe_{0.8}Mo_{0.2})MoO_6$ perovskite in $Mn_2Fe_{1+x}Mo_{1-x}O_6$, raises a new possibility. The Ni_3TeO_6-type Mn_2FeMoO_6 is known to be stabilized by the spin structure,[15] while the absence of solid solutions and the formation of a new perovskite line phase $Mn_2(Fe_{0.8}Mo_{0.2})MoO_6$ could be a synergy of thermodynamics, crystal, and spin structure (mixed-valence $Mo^{4+/5+}$) based energetic effect. Further theoretical calculations are necessary to better understand these correlations and guide the design of new

DOI: 10.1021/acs.chemmater.8b00250
Chem. Mater. 2018, 30, 4508−4514

polar and magnetic corundum phases and transition-metal-only double perovskites, which are important for spintronic applications.

■ ASSOCIATED CONTENT

Supporting Information

The Supporting Information is available free of charge on the ACS Publications website at DOI: 10.1021/acs.chemmater.8b00250.

Line phase mining, Mn− and Fe−K edge and pre-edge XANES figures, detailed magnetism and magnetic phase diagram analysis (PDF)

Crystallographic information file for Mn2Fe.8Mo1.2O6_300K (CIF)

■ AUTHOR INFORMATION

Corresponding Authors

*E-mail: greenbla@chem.rutgers.edu.

*E-mail: limanrong@mail.sysu.edu.cn.

ORCID

Man-Rong Li: 0000-0001-8424-9134

Peter W. Stephens: 0000-0002-8311-7305

Martha Greenblatt: 0000-0002-1806-2766

Notes

The authors declare no competing financial interest.

The supporting crystallographic information file may also be obtained from FIZ Karlsruhe, 76344 Eggenstein-Leopoldshafen, Germany (e-mail: crysdata@fiz-karlsruhe.de), on quoting the deposition number CSD-433446.

■ ACKNOWLEDGMENTS

This work was supported by the NSF-DMR-1507252 grant (USA) and the "One Thousand Youth Talents" Program (China). Use of the NSLS, Brookhaven National Laboratory, was supported by the DOE BES (DE-AC02-98CH10886). M.R. thanks the Spanish *Juan de la Cierva* grant FPDI-2013-17582. Work on IOP, CAS, was supported by NSFC and MOST grants. A portion of this research at ORNL's Spallation Neutron Source was sponsored by the Scientific User Facilities Division, Office of Basic Energy Sciences, US Department of Energy.

■ REFERENCES

(1) Markkula, M.; Arevalo-Lopez, A. M.; Kusmartseva, A.; Rodgers, J. A.; Ritter, C.; Wu, H.; Attfield, J. P. Incommensurate spin order in the metallic perovskite $MnVO_3$. *Phys. Rev. B: Condens. Matter Mater. Phys.* **2011**, *84*, 094450.

(2) Belik, A. A.; Yi, W. High-pressure synthesis, crystal chemistry and physics of perovskites with small cations at the A site. *J. Phys.: Condens. Matter* **2014**, *26*, 163201.

(3) Long, Y. W.; Hayashi, N.; Saito, T.; Azuma, M.; Muranaka, S.; Shimakawa, Y. Temperature-induced A-B intersite charge transfer in an A-site-ordered $LaCu_3Fe_4O_{12}$ perovskite. *Nature* **2009**, *458*, 60−63.

(4) Chen, W.-t.; Mizumaki, M.; Seki, H.; Senn, M. S.; Saito, T.; Kan, D.; Attfield, J. P.; Shimakawa, Y. A half-metallic A- and B-site-ordered quadruple perovskite oxide $CaCu_3Fe_2Re_2O_{12}$ with large magnetization and a high transition temperature. *Nat. Commun.* **2014**, *5*, 3909.

(5) Ovsyannikov, S. V.; Abakumov, A. M.; Tsirlin, A. A.; Schnelle, W.; Egoavil, R.; Verbeeck, J.; Van Tendeloo, G.; Glazyrin, K. V.; Hanfland, M.; Dubrovinsky, L. Perovskite-like Mn_2O_3: a path to new manganites. *Angew. Chem., Int. Ed.* **2013**, *52*, 1494−1498.

(6) Ovsyannikov, S. V.; Karkin, A. E.; Morozova, N. V.; Shchennikov, V. V.; Bykova, E.; Abakumov, A. M.; Tsirlin, A. A.; Glazyrin, K. V.; Dubrovinsky, L. A Hard Oxide Semiconductor with A Direct and Narrow Bandgap and Switchable p−n Electrical Conduction. *Adv. Mater.* **2014**, *26*, 8185−8191.

(7) Li, M.-R.; Retuerto, M.; Deng, Z.; Stephens, P. W.; Croft, M.; Huang, Q.; Wu, H.; Deng, X.; Kotliar, G.; Sánchez-Benítez, J.; Hadermann, J.; Walker, D.; Greenblatt, M. Giant Magnetoresistance in the Half-Metallic Double-Perovskite Ferrimagnet Mn_2FeReO_6. *Angew. Chem., Int. Ed.* **2015**, *54*, 12069−12073.

(8) Arévalo-López, A. M.; McNally, G. M.; Attfield, J. P. Large Magnetization and Frustration Switching of Magnetoresistance in the Double-Perovskite Ferrimagnet Mn_2FeReO_6. *Angew. Chem., Int. Ed.* **2015**, *54*, 12074−12077.

(9) Arevalo-Lopez, A. M.; Stegemann, F.; Attfield, J. P. Competing antiferromagnetic orders in the double perovskite Mn_2MnReO_6 (Mn_3ReO_6). *Chem. Commun.* **2016**, *52*, 5558−5560.

(10) Li, M.-R.; Hodges, J. P.; Retuerto, M.; Deng, Z.; Stephens, P. W.; Croft, M. C.; Deng, X.; Kotliar, G.; Sánchez-Benítez, J.; Walker, D.; Greenblatt, M. Mn_2MnReO_6: Synthesis and Magnetic Structure Determination of a New Transition-Metal-Only Double Perovskite Canted Antiferromagnet. *Chem. Mater.* **2016**, *28*, 3148−3158.

(11) Mathieu, R.; Ivanov, S. A.; Solovyev, I. V.; Bazuev, G. V.; Anil Kumar, P.; Lazor, P.; Nordblad, P. Mn_2FeSbO_6: A ferrimagnetic ilmenite and an antiferromagnetic perovskite. *Phys. Rev. B: Condens. Matter Mater. Phys.* **2013**, *87*, 014408.

(12) Dos santos-Garcia, A. J.; Solana-Madruga, E.; Ritter, C.; Avila-Brande, D.; Fabelo, O.; Saez-Puche, R. Synthesis, structures and magnetic properties of the dimorphic Mn_2CrSbO_6 oxide. *Dalton Trans.* **2015**, *44*, 10665−10672.

(13) Akizuki, Y.; Yamada, I.; Fujita, K.; Nishiyama, N.; Irifune, T.; Yajima, T.; Kageyama, H.; Tanaka, K. A-Site-Ordered Perovskite $MnCu_3V_4O_{12}$ with a 12-Coordinated Manganese(II). *Inorg. Chem.* **2013**, *52*, 11538−11543.

(14) Akizuki, Y.; Yamada, I.; Fujita, K.; Taga, K.; Kawakami, T.; Mizumaki, M.; Tanaka, K. Rattling in the Quadruple Perovskite $CuCu_3V_4O_{12}$. *Angew. Chem., Int. Ed.* **2015**, *54*, 10870−10874.

(15) Li, M.-R.; Retuerto, M.; Walker, D.; Sarkar, T.; Stephens, P. W.; Mukherjee, S.; Dasgupta, T. S.; Hodges, J. P.; Croft, M.; Grams, C. P.; Hemberger, J.; Sánchez-Benítez, J.; Huq, A.; Saouma, F. O.; Jang, J. I.; Greenblatt, M. Magnetic-Structure-Stabilized Polarization in an Above-Room-Temperature Ferrimagnet. *Angew. Chem., Int. Ed.* **2014**, *53*, 10774−10778.

(16) Li, M.-R.; Retuerto, M.; Stephens, P. W.; Croft, M.; Sheptyakov, D.; Pomjakushin, V.; Deng, Z.; Akamatsu, H.; Gopalan, V.; Sánchez-Benítez, J.; Saouma, F. O.; Jang, J. I.; Walker, D.; Greenblatt, M. Low-Temperature Cationic Rearrangement in a Bulk Metal Oxide. *Angew. Chem., Int. Ed.* **2016**, *55*, 9862−9867.

(17) Walker, D.; Carpenter, M. A.; Hitch, C. M. Some simplifications to multianvil devices for high pressure experiments. *Am. Mineral.* **1990**, *75*, 1020−1028.

(18) Li, M.-R.; Stephens, P. W.; Retuerto, M.; Sarkar, T.; Grams, C. P.; Hemberger, J.; Croft, M. C.; Walker, D.; Greenblatt, M. Designing Polar and Magnetic Oxides: Zn_2FeTaO_6 - in Search of Multiferroics. *J. Am. Chem. Soc.* **2014**, *136*, 8508−8511.

(19) Li, M.-R.; Walker, D.; Retuerto, M.; Sarkar, T.; Hadermann, J.; Stephens, P. W.; Croft, M.; Ignatov, A.; Grams, C. P.; Hemberger, J.; Nowik, I.; Halasyamani, P. S.; Tran, T. T.; Mukherjee, S.; Dasgupta, T. S.; Greenblatt, M. Polar and Magnetic Mn_2FeMO_6 (M = Nb, Ta) with $LiNbO_3$-type Structure: High-Pressure Synthesis. *Angew. Chem., Int. Ed.* **2013**, *52*, 8406−8410.

(20) Retuerto, M.; Li, M.-R.; Stephens, P. W.; Sánchez-Benítez, J.; Deng, X.; Kotliar, G.; Croft, M. C.; Ignatov, A.; Walker, D.; Greenblatt, M. Half-Metallicity in Pb_2CoReO_6 Double Perovskite and High Magnetic Ordering Temperature in Pb_2CrReO_6 Perovskite. *Chem. Mater.* **2015**, *27*, 4450−4458.

(21) Li, M.-R.; Retuerto, M.; Deng, Z.; Sarkar, T.; Sánchez-Benítez, J.; Croft, M. C.; Dasgupta, T. S.; Das, T.; Tyson, T. A.; Walker, D.; Greenblatt, M. Strong Electron Hybridization and Fermi-to-Non-Fermi Liquid Transition in $LaCu_3Ir_4O_{12}$. *Chem. Mater.* **2015**, *27*, 211−217.

DOI: 10.1021/acs.chemmater.8b00250
Chem. Mater. 2018, 30, 4508−4514

(22) Li, M.-R.; Croft, M.; Stephens, P. W.; Ye, M.; Vanderbilt, D.; Retuerto, M.; Deng, Z.; Grams, C. P.; Hemberger, J.; Hadermann, J.; Li, W.-M.; Jin, C.-Q.; Saouma, F. O.; Jang, J. I.; Akamatsu, H.; Gopalan, V.; Walker, D.; Greenblatt, M. Mn_2FeWO_6: A New Ni_3TeO_6-Type Polar and Magnetic Oxide. *Adv. Mater.* **2015**, *27*, 2177−2181.
(23) Campbell, B. J.; Stokes, H. T.; Tanner, D. E.; Hatch, D. M. ISODISPLACE: a web-based tool for exploring structural distortions. *J. Appl. Crystallogr.* **2006**, *39*, 607−614.
(24) Toby, B. EXPGUI, a graphical user interface for GSAS. *J. Appl. Crystallogr.* **2001**, *34*, 210−213.
(25) Rietveld, H. A profile refinement method for nuclear and magnetic structures. *J. Appl. Crystallogr.* **1969**, *2*, 65−71.
(26) Momma, K.; Izumi, F. VESTA 3 for three-dimensional visualization of crystal, volumetric and morphology data. *J. Appl. Crystallogr.* **2011**, *44*, 1272−1276.
(27) Croft, M.; Sills, D.; Greenblatt, M.; Lee, C.; Cheong, S. W.; Ramanujachary, K. V.; Tran, D. Systematic Mn d-configuration change in the $La_{1-x}Ca_xMnO_3$ system: A Mn K-edge XAS study. *Phys. Rev. B: Condens. Matter Mater. Phys.* **1997**, *55*, 8726−8732.
(28) Veith, G. M.; Lobanov, M. V.; Emge, T. J.; Greenblatt, M.; Croft, M.; Stowasser, F.; Hadermann, J.; Tendeloo, G. V. Synthesis and characterization of the new Ln_2FeMoO_7 (Ln = Y, Dy, Ho) compounds. *J. Mater. Chem.* **2004**, *14*, 1623−1630.
(29) Veith, G. M.; Greenblatt, M.; Croft, M.; Ramanujachary, K. V.; Hattrick-Simpers, J.; Lofland, S. E.; Nowik, I. Synthesis and Characterization of $Sr_3FeMoO_{6.88}$: An Oxygen-Deficient 2D Analogue of the Double Perovskite Sr_2FeMoO_6. *Chem. Mater.* **2005**, *17*, 2562−2567.
(30) Whaley, L. W.; Lobanov, M. V.; Sheptyakov, D.; Croft, M.; Ramanujachary, K. V.; Lofland, S.; Stephens, P. W.; Her, J.-H.; Van Tendeloo, G.; Rossell, M.; Greenblatt, M. $Sr_3Fe_{5/4}Mo_{3/4}O_{6.9}$, an $n = 2$ Ruddlesden−Popper Phase: Synthesis and Properties. *Chem. Mater.* **2006**, *18*, 3448−3457.
(31) Huang, Y.-H.; Liang, G.; Croft, M.; Lehtimäki, M.; Karppinen, M.; Goodenough, J. B. Double-Perovskite Anode Materials Sr_2MMoO_6 (M = Co, Ni) for Solid Oxide Fuel Cells. *Chem. Mater.* **2009**, *21*, 2319−2326.
(32) Retuerto, M.; Li, M. R.; Go, Y. B.; Ignatov, A.; Croft, M.; Ramanujachary, K. V.; Hadermann, J.; Hodges, J. P.; Herber, R. H.; Nowik, I.; Greenblatt, M. Magnetic and structural studies of the multifunctional material $SrFe_{0.75}Mo_{0.25}O_{3-\delta}$. *Inorg. Chem.* **2012**, *51*, 12273−12280.
(33) Zeng, Z.; Fawcett, I. D.; Greenblatt, M.; Croft, M. Large magnetoresistance in double perovskite $Sr_2Cr_{1.2}Mo_{0.8}O_{6-\delta}$. *Mater. Res. Bull.* **2001**, *36*, 705−715.
(34) Kobayashi, K. I.; Kimura, T.; Sawada, H.; Terakura, K.; Tokura, Y. Room-temperature magnetoresistance in an oxide material with an ordered double-perovskite structure. *Nature* **1998**, *395*, 677−680.
(35) Solana-Madruga, E.; Dos santos-Garcia, A. J.; Arevalo-Lopez, A. M.; Avila-Brande, D.; Ritter, C.; Attfield, J. P.; Saez-Puche, R. High pressure synthesis of polar and non-polar cation-ordered polymorphs of Mn_2ScSbO_6. *Dalton Trans.* **2015**, *44*, 20441−20448.
(36) Shannon, R. Revised effective ionic radii and systematic studies of interatomic distances in halides and chalcogenides. *Acta Crystallogr., Sect. A: Cryst. Phys., Diffr., Theor. Gen. Crystallogr.* **1976**, *32*, 751−767.
(37) Wei, G.-Z.; Liang, Y.-Q.; Zhang, Q.; Xin, Z.-H. Magnetic properties of mixed-spin Ising systems in a longitudinal magnetic field. *J. Magn. Magn. Mater.* **2004**, *271*, 246−253.
(38) Deviren, B.; Bati, M.; Keskin, M. The effective-field study of a mixed spin-1 and spin-5/2 Ising ferrimagnetic system. *Phys. Scr.* **2009**, *79* (6), 065006.
(39) Anshul, A.; Aloysius, R. P.; Gupta, A.; Basheed, G. A. Magnetodielectric coupling in epitaxial Nd_2CoMnO_6 thin films with double perovskite structure. *J. Appl. Phys.* **2014**, *115*, 084106.
(40) Sazonov, A. P.; Troyanchuk, I. O.; Kozlenko, D. P.; Balagurov, A. M.; Sikolenko, V. V. Magnetic ordering in the $Nd_2CoMnO_{6+\delta}$ perovskite system. *J. Magn. Magn. Mater.* **2006**, *302*, 443−447.
(41) Hemberger, J.; Lobina, S.; Krug von Nidda, H. A.; Tristan, N.; Ivanov, V. Y.; Mukhin, A. A.; Balbashov, A. M.; Loidl, A. Complex interplay of 3*d* and 4*f* magnetism in $La_{1-x}Gd_xMnO_3$. *Phys. Rev. B: Condens. Matter Mater. Phys.* **2004**, *70*, 024414.
(42) da Silva, C. A.; Silva, R. S.; Plaza, E. J. R.; Moreno, N. O. Magnetic State and Magnetocaloric Effect of $SmMnO_3$. *J. Supercond. Novel Magn.* **2013**, *26*, 2497−2499.
(43) Kobayashi, K. I.; Kimura, T.; Tomioka, Y.; Sawada, H.; Terakura, K.; Tokura, Y. Intergrain tunneling magnetoresistance in polycrystals of the ordered double perovskite Sr_2FeReO_6. *Phys. Rev. B: Condens. Matter Mater. Phys.* **1999**, *59*, 11159−11162.
(44) Sriti, F.; Maignan, A.; Martin, C.; Raveau, B. Influence of Fe-Site Substitutions upon Intragrain and Intergrain Magnetoresistance in the Double-Perovskite Ba_2FeMoO_6. *Chem. Mater.* **2001**, *13*, 1746−1751.
(45) Cai, G.-H.; Greenblatt, M.; Li, M.-R. Polar Magnets in Double Corundum Oxides. *Chem. Mater.* **2017**, *29*, 5447−5457.

DOI: 10.1021/acs.chemmater.8b00250
Chem. Mater. 2018, 30, 4508−4514